Charge density wave phase of VSe_2 revisited

Wouter Jolie,[1,2,*] Timo Knispel,[1] Niels Ehlen,[1] Konstantin Nikonov,[1,3] Carsten Busse,[1,2,4] Alexander Grüneis,[1] and Thomas Michely[1]

[1]*II. Physikalisches Institut, Universität zu Köln, Zülpicher Straße 77, 50937 Köln, Germany*

[2]*Institut für Materialphysik, Westfälische Wilhelms-Universität Münster, Wilhelm-Klemm-Straße 10, 48149 Münster, Germany*

[3]*Kurnakov Institute of General and Inorganic Chemistry of the Russian Academy of Sciences, 119991 Moscow, Russia*

[4]*Department Physik, Universität Siegen, 57068 Siegen, Germany*

(Received 2 October 2018; revised manuscript received 21 January 2019; published 12 March 2019)

Scanning tunneling microscopy and spectroscopy are used to image the charge density wave at the surface of cleaved VSe_2 and to probe its local density of states at 5 K. The main features in the spectrum are linked to the contributions of the *p*-like and *d*-like bands of VSe_2 found in angle-resolved photoemission spectroscopy and tight-binding calculations. Different from previous tunneling spectroscopy work, we find a narrow partial gap at the Fermi level that we associate with the charge density wave phase. The energy scale of the gap found in the experiment is in good agreement with the charge density wave transition temperature of VSe_2, under the assumption of weak electron-phonon coupling, consistent with the Peierls model of Fermi surface nesting. The role of defects is investigated, which reveals that the partial gap in the density of states and hence the charge density wave itself is extremely stable, though the order, phase, and amplitude of the charge density waves on the surface are strongly perturbed by defects.

DOI: 10.1103/PhysRevB.99.115417

I. INTRODUCTION

Layered materials such as transition metal dichalcogenides (TMDCs) tend to be electronically unstable due to their quasi-two-dimensional structure [1], which in combination with many-body interactions can lead to exotic phase transitions such as superconductivity [2], charge density waves (CDWs) [3], or orbital order [4] at low temperatures. The origin of the phase transitions in TMDCs is often not uniquely identified because several factors—such as the near-perfect nesting condition due to the reduced dimensionality and strong electron-phonon coupling—are present. The various contributions lead to an interplay that is theoretically still not well understood [3]. Prominent examples are TaS_2 [4], $TaSe_2$ [5], $TiSe_2$ [6], $NbSe_2$ [7], and VSe_2.

The TMDC 1T-VSe_2 has promising intrinsic photocatalytic properties [8], it was shown to improve the performance of CdTe solar cells [9], and nanosheets of 1T-VSe_2 display photoluminescence [10]. 1T-VSe_2 is metallic with a strong in-plane and weak out-of-plane dispersion due to the different intra- and interlayer coupling strengths [11]. It undergoes two CDW phase transitions at $T \approx 110\,\mathrm{K}$ and $T \approx 80\,\mathrm{K}$. The CDW is three-dimensional, with a commensurate in-plane CDW wave vector $\mathbf{q}_{\mathrm{CWD}} = 0.250\,\mathbf{a}^*$ ($\mathbf{a}^*$ is an in-plane primitive translation of the reciprocal lattice) [12–14] and an incommensurate out-of-plane component [13,14]. The in-plane commensurability of the CDW has been confirmed with scanning tunneling microscopy (STM), whereas it provides no information on the out-of-plane component.

Recently renewed interest in the physics of VSe_2 arose through the ability to prepare thin films of well-defined thickness down to the monolayer [15–20], which display distinctly different properties from the bulk material, as the following three examples illuminate: First, ferromagnetism, absent in VSe_2 bulk, was proposed [18], but also refuted [19]. Second, much higher CDW transition temperatures were reported for the monolayer ranging from 121 K [18], over 140 K [19], up to 350 K [20], a variety of lower and higher CDW temperatures for thin films in the nm to 10 nm range [15,16], and a nonmonotonic dependence of the CDW transition temperature on sample thickness [17]. Third, a fully gapped band structure was reported for the monolayer at low temperatures with CDW gaps of $2\Delta = 55$ meV obtained by scanning tunneling spectroscopy (STS) [18], and estimates from angle-resolved photoemission spectroscopy (ARPES) range between $\Delta = (30 \pm 5)$ meV [19] and $\Delta = (9 \pm 4)$ meV [20].

The scatter in the VSe_2 data may be understandable in view of the challenges to prepare well-defined monolayers and thin films as well as the increasingly important substrate effect when the thickness decreases. Nevertheless, even for the bulk VSe_2 unresolved issues and substantial scatter in the reported data prevail: Using ARPES, Terashima *et al.* [21] reported a partial gap opening (often referred to as pseudogap) on the electronlike Fermi surface (FS) centered at the $M(L)$ point, which they attributed to the CDW formation. Their results point to a CDW gap $2\Delta = 80$–100 meV. Sato *et al.* [22] showed that the pseudogap opens only at certain wave vectors perpendicular to the layers, due to the dispersive behavior out-of-plane, and they found a shift in the peak intensity away from the Fermi energy of 20–30 meV resulting in a gap of $2\Delta = 40$–60 meV. Strocov *et al.* [11] confirmed the three-dimensional (3D) nesting vector with high-resolution

*wjolie@ph2.uni-koeln.de

ARPES measurements, but they did not report any gap opening.

Using STS, the CDW gap is directly accessible, as STS probes the occupied and unoccupied density of states (DOS). Wang *et al.* [23] reported a gap of $2\Delta = 80$ meV at $T = 4.2$ K, Ekvall *et al.* [24] found a gap of $2\Delta = 160$ meV at $T = 60$ K for cleaved bulk VSe_2, and Pásztor *et al.* [17] did not find any gap-related feature at 78 K.

Besides the nature and size of the CDW gap, there is another ambiguous result in the literature. Triggered by an initial report by Eaglesham *et al.* [14], some authors noticed also in STM micrographs a lack of sixfold symmetry in the CDW pattern with domains in certain preferred directions [25,26], while others emphasized the isotropic appearance of the CDW pattern [27].

In the present paper, we explain the origin of the scatter in the published data for CDW gaps of cleaved VSe_2 crystals, and we clarify the symmetry of the in-plane (4×4) CDW pattern. Our comprehensive analysis is based on STM and STS data obtained at 5 K, far below the two CDW transitions. It is supplemented by ARPES data and tight-binding simulations that uncover the different contributions observed in STS spectra. We find that the scatter in the data can plausibly be explained by different assignments of STS features to the band structure of VSe_2. It can be overcome by an operative and reproducible method to extract the size of the CDW gap from STS data. Finally, we discuss the role of defects for the CDW pattern.

II. METHODS

Following the method of Ohtani *et al.* [28], VSe_2 single crystals were grown using the chemical vapor transport method with iodine and chlorine as a transport agent [29]. The crystals are gray, shiny, hexagonal-shaped thin platelets of approximately 3–5 mm^2 size. Excess Se, iodine, and chlorine were removed via bathing the crystals in ethanol and heating in vacuum. The data shown in the present paper stem from crystals grown with iodine as a transport agent, except for Fig. 6(d) where chlorine was used.

For STM the platelet-shaped VSe_2 crystals were mounted with their backside to the STM sample holder by using silver-filled epoxy glue. On their topside a metal pin was attached normal to the crystal surface using the same glue. Sample cleavage resulted from moving the metal pin against an edge. During and after cleavage, the pressure in the STM ultrahigh-vacuum preparation chamber was $p < 2 \times 10^{-10}$ mbar. The cleaved sample surface was moved into the STM bath cryostat within a few minutes, where the pressure was $p < 10^{-11}$ mbar.

STM and STS were performed at 5 K using a Createc low-temperature STM system with a modified beetle-type STM [30]. Constant-height dI/dV point spectra as well as constant-current dI/dV maps were recorded, with V being the bias voltage applied to the sample and I the tunneling current. We refer to them as STS spectra and STS maps in the following. Both were measured with a lock-in amplifier using a modulation voltage V_{mod} of 4–10 mV and a frequency of $f = 777$ Hz. The STS maps and STM topographs were analyzed using the WSxM software [31].

ARPES measurements were performed at the BaDElPh beamline [32] of the Elettra synchrotron in Trieste (Italy) using p-polarized light in a horizontal slit geometry at 20 K. As for the STM experiments, the crystal was cleaved *in situ* in a pressure $p < 10^{-10}$ mbar. High-symmetry directions were determined by low-energy electron diffraction (LEED). Energy dispersion curves through the ARPES data were taken at points in the full three-dimensional Brillouin zone (see the supplemental material [33]). The intensity maxima of these curves are extracted for the tight-binding fitting procedure that is described in the following. The raw ARPES data are shown elsewhere [34].

Our TB model for bulk VSe_2 is based on an existing model for monolayer 1H-MoS_2 [35,36] that we have adjusted to represent the 1T-VSe_2 bulk structure. This is accomplished by flipping the direction of the transition-metal–chalcogenide hopping for one of the sulfur planes and by adding out-of-plane hopping terms in the Hamiltonian. The spin-independent, orthogonal tight-binding calculations were conducted using a basis set of 11 p- and d-orbitals for the Hilbert space. In short, the five $3d$ orbitals are located at the vanadium site in the unit cell, and three $4p$ orbitals are located at each of the two selenium sites in the unit cell. For the individual Se and V planes, a nearest-neighbor approximation was used, and additional hopping between the planes was introduced by using nearest-neighbor hopping from V to the lower and the upper Se plane, respectively. To significantly reduce the parameter space, we employ the Slater-Koster approximation for the hopping terms [37] and use symmetry to minimize the amount of independent on-site energies. For simplicity, we used the parameters for MoS_2 from the literature [36] as a starting point for our fit to the ARPES band structure, since the relative size of the hopping terms is expected to be of the same order of magnitude in MoS_2 and VSe_2. We find that the nearest-neighbor approximation is sufficient for a good fit to the experiment. Using the eigenvector of the Hamiltonian, we extract the character of the bands (d- or p-type). The density of states was obtained from the band structure by integrating over the Brillouin zone. Angle integration of the ARPES data would provide an inferior estimate for the occupied density of states because of energy and polarization-dependent matrix element effects. Compared to *ab initio* density functional theory calculations, the TB method provides the advantage of a precise fit to experimental data. This is useful when considering the orbital character of a given feature in the STS current or for future calculations of the experimental bare spin susceptibility.

III. STRUCTURAL AND ELECTRONIC PROPERTIES OF VANADIUM DISELENIDE

Atomically resolved STM images of the surface of VSe_2 are shown in Figs. 1(a) and 1(b). The surface atoms appear bright or dark, depending on the tip and tunneling conditions. While the STM contrast in Fig. 1(b) is the most common one, it is not trivial to assign V or Se to the atomic positions: though the DOS near the Fermi level is governed by V d-states [27], the surface consists of Se atoms, which are therefore closer to the tip [25,27]. In both STM images, a pronounced (4×4) periodic structure with respect to the atomic lattice is visible

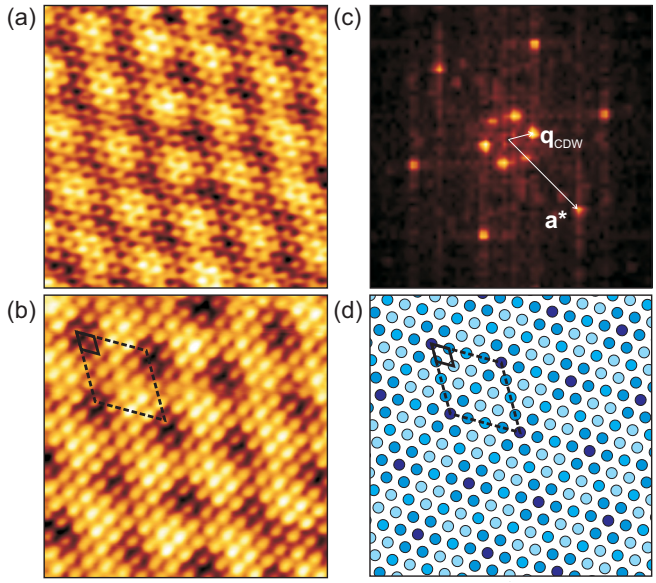

FIG. 1. In-plane structure of VSe_2: (a) STM image of VSe_2 ($U = -0.75$ V, $I = 0.2$ nA, image size 6.2×6.2 nm^2). (b) STM image recorded with a different tip showing another atomic contrast ($U = -0.2$ V, $I = 0.5$ nA, image size 5.3×5.3 nm^2). (c) FT of the STM image shown in (a). The large arrow represents a reciprocal-lattice vector of VSe_2, while the small arrow represents a reciprocal-lattice vector of the CDW. (d) Ball model of the (4×4) structure, in which the balls denote atoms and the different colors visualize the superstructure. The primitive unit cell of the lattice and the superstructure are displayed with a continuous and dashed rhomboid, respectively.

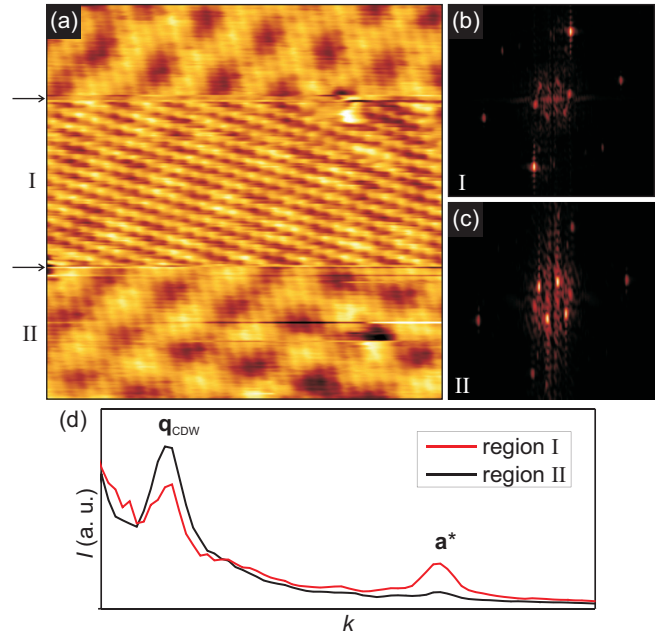

FIG. 2. Influence of the tip on the CDW modulation: (a) STM image of VSe_2 ($U = -0.2$ V, $I = 0.2$ nA, image size 8.5×8.5 nm^2). Two pronounced tip changes are marked with arrows. (b) FT of region I shown in (a). (c) FT of region II. (d) Radial average of both FTs. The CDW and atomic peaks are labeled.

and attributed to the CDW of VSe_2. The commensurability is verified in areas free of defects by counting the atoms along the crystallographic directions and then dividing by the number of CDW periods. With this method one can minimize the systematic errors of the STM, which are otherwise of the order of 5%. The resulting periodicity is $(4.00 \pm 0.07)a$, with a defined as the in-plane lattice constant of VSe_2, i.e., the structure is commensurate within the error margin.

The CDW period is also visible in the Fourier transform (FT) of STM images that give direct access to reciprocal space. An example is shown in Fig. 1(c), which represents the FT of Fig. 1(a). We find six outer spots that are attributed to the reciprocal-lattice vectors of the VSe_2 surface. One of them is indicated in Fig. 1(c), labeled $\mathbf{a}^*$. The six inner spots stem from the (4×4) periodicity of the CDW, which corresponds to $|\mathbf{a}^*|/4$ in reciprocal space. One is also sketched in Fig. 1(c), labeled $\mathbf{q}_{CDW}$. A ball model of the CDW structures is displayed in Fig. 1(d), in which the balls represent the surface atoms of VSe_2 and the different colors visualize the (4×4) structure of the CDW. The unit cells of VSe_2 and of the CDW are indicated.

In agreement with a symmetry break proposed on the basis of transmission electron microscopy in the low-temperature CDW phase by Eaglesham *et al.* [14], Coleman *et al.* [25] and Giambattista *et al.* [26] find a pronounced unidirectional enhancement of the CDW pattern. In contrast, Kim *et al.* [27] observe a sixfold rotational symmetry. The STM images in Figs. 1(a) and 1(b) point to a commensurate, periodic structure with sixfold rotational symmetry. We observed that depending on the tip state, scanning the same area may lead to drastic changes of the CDW symmetry. Figure 2(a) demonstrates the influence of two tip changes during an STM scan. The image was scanned from top to bottom, leading to two pronounced horizontal discontinuities (arrows). The two areas labeled I and II imaged with a different tip apex are further analyzed in the following. Their FTs are displayed in Figs. 2(b) and 2(c). In the FT of region I, the two CDW spots on a line close to horizontal are the brightest, while they are the darkest in the FT of region II; compare Figs. 2(b) and 2(c). Hence the most pronounced periodicity in region I becomes the weakest in region II. This leads to the conclusion that the reported symmetry breaking [25,26] is likely to result from nonisotropic tips rather than from the CDW itself. Additionally, defects can locally break the sixfold symmetry and, as a consequence, lead to a distorted CDW, as shown below.

The tip apex can not only reduce the symmetry of the CDW, but also strongly affect the intensity ratio between atomic and CDW peaks. This can be illustrated by taking the radial average of both FTs; see Fig. 2(d). The relative peak heights in the FT corresponding to atomic and CDW periodicities show strong variation depending on the tip state: the peak related to the atomic corrugation in region I is much higher than in region II, while the opposite is true for the CDW peak. Such effects may be of relevance, when physical quantities like the CDW transition temperature are estimated on the basis of the intensity ratios [17].

An STS spectrum that measures the LDOS present at the surface of VSe_2 is shown in Fig. 3. The dI/dV signal is displayed in Fig. 3(a). Several features are present that can be highlighted by dividing the dI/dV signal by I/V. This is done

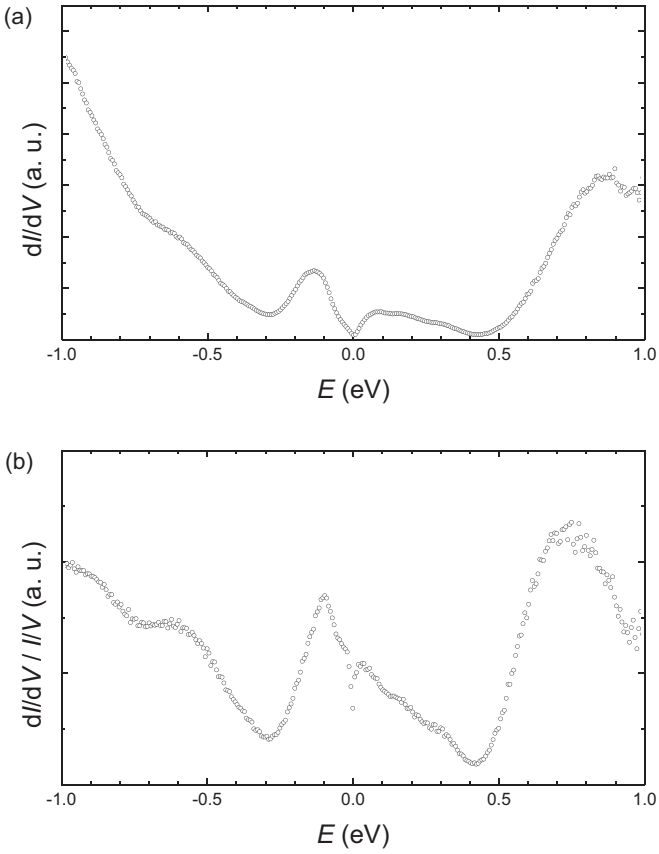

FIG. 3. LDOS of VSe_2: (a) STS spectrum of VSe_2 ($U_{stab} = -1$ V, $I_{stab} = 1$ nA). (b) Normalized STS spectrum. We find peaks around -0.1 and 0.75 eV, dips around the Fermi level and 0.45 eV, and shoulders at -0.8 and -0.5 eV.

in Fig. 3(b) using the data of Fig. 3(a). The normalization cancels out the exponential divergence of the transmission probability in the spectroscopic signal, whereby the spectroscopic features (peaks, valleys) are more pronounced and slightly shifted toward $E = 0$ in Fig. 3(b) [38,39]. Hence we focus on the features of the normalized spectrum in the following. We find a peak around $E = -0.1$ eV that is attributed to the d-states of V near the Γ point [40], in line with the STS spectra reported by Refs. [17,24]. In addition, we find dips around $E = -0.3$ and 0.4 eV and around the Fermi level, together with a pronounced shoulder around $E = -0.5$ eV and a broad peak around $E = 0.75$ eV. The overall shape of the spectrum is in accordance with the observation of Pásztor *et al.* in Ref. [17] aside from the dip at the Fermi level, which is much narrower than in previous reports [23,24]. In the following, we will discuss all these features and link them to their corresponding bands found in tight-binding calculations of VSe_2, if present.

The band structure of VSe_2 obtained from tight-binding calculations is presented in Fig. 4(a). The bands were optimized to match experimental ARPES and STS results measured on samples from the same crystal growth batch. The red-colored dots in the background represent Lorentzian peak fits to energy distribution curves of the ARPES data [33], while the dots colored from dark blue to yellow are the corresponding theoretical fits using our tight-binding model. The color of the bands depends on their orbital character, which ranges from fully p-type (dark blue) to fully d-type (yellow). The band that crosses the Fermi level is attributed to the d-band of V mentioned above, while additional bands derived from the p-orbitals of Se are located at slightly lower energies. The occupied band structure is in overall agreement with the literature [11]. While there is good agreement between ARPES and the tight-binding simulation in the occupied states, a lack of constraints to the fit parameters for the unoccupied band structure may lead to strong deviations there, as will be discussed below.

The tight-binding Hamiltonian can be used to compute the DOS of VSe_2, which is shown in Fig. 4(b). The blue curve represents the total DOS, which is divided into the DOS arising from p-orbitals (dark blue) and d-orbitals (yellow), respectively. We can now compare the simulated DOS with the STS spectrum that is plotted in green in Fig. 4(b). The peak seen in the STS spectrum at $E = -0.1$ eV is at the location where we find a peak in the tight-binding simulated DOS. The main contribution to this peak stems from the d-states of V near the Fermi energy. The dip at $E = -0.3$ eV in the occupied states of the STS spectrum is located at the crossover between d-states and p-states, though it is much more pronounced in the STS spectrum. The shoulder at $E = -0.5$ eV is likely to be related to the additional contribution from the holelike band at the Γ point that has a maximum at the corresponding energy.

While there is an overall good agreement in the occupied states, the situation is different at energies above the chemical potential. The peak measured with STS at $E = 0.75$ eV is likely to stem from the unoccupied bands, though their contribution to the simulated DOS forms a peak at much higher energies, around $E \approx 1$ eV. The dip at $E = 0.4$ eV between the peaks in the unoccupied states and near to the Fermi energy would then represent the minimum between the different d-bands that is also visible in the simulation, though much larger in size due to the high energies of the unoccupied d-bands. DFT calculations indeed show that the unoccupied bands tend to be lower in energy [11], in good agreement with our and reported STS data [17]. The difference in energy is attributed to the fact that only the occupied bands can be properly fitted to ARPES data, while no information on the unoccupied states is known from this experimental technique.

Though the main features of the STS spectra can be attributed to the states of VSe_2, one is not reproduced by the tight-binding calculation, namely the pronounced dip found at the Fermi level. It is hence attributed to the CDW gap 2Δ that opens in the CDW phase. Figure 5 shows a high-resolution STS spectrum measured around the Fermi level. The feature is rather continuous instead of abrupt, making it difficult to extract 2Δ. In addition, the peak arising from the d-states tends to mask the dip and leads to a pronounced asymmetry. To obtain a reproducible estimate for 2Δ, we proceed as follows: The spectrum is fitted in a small energy range around the Fermi level (omitting the gap) with a third-order polynomial function to deconvolute the gap from the peak arising from the d-states at the Γ point, which do not contribute to the CDW formation. The green line shows the polynomial fit to the spectrum in Fig. 5. This can be considered as the DOS at high temperatures, where no CDW and consequently

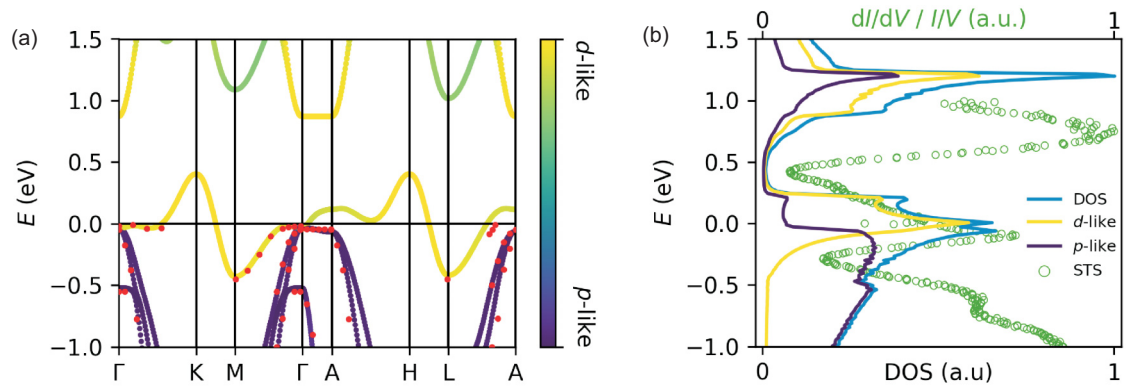

FIG. 4. Tight-binding calculation of the bands and DOS of VSe_2: (a) Band structure of VSe_2 in high-symmetry directions. The color scale encodes the orbital character of the bands ranging from pure d- (yellow) to pure p-orbital character (dark blue). ARPES intensity maxima used for the tight-binding fit are denoted by red colored dots. (b) Comparison of the tight-binding calculated DOS (medium blue line) and the STS spectrum (green dots). The contribution of d-states to the tight-binding DOS is shown as a yellow line, while the contribution of the p-states is shown as a dark blue line.

no gap is present. The difference between these two curves (defined as DOS_{CDW}) is calculated and shown in the inset. By assuming that DOS_{CDW} is only related to the CDW gap opening 2Δ, it simply shows the suppression in the DOS due to the CDW phase transition. This feature can be fitted with a Gaussian to extract its full width at half-maximum (FWHM), which then gives a measure of the CDW gap. The red curve in the inset of Fig. 5 represents the Gaussian fit, with its FWHM indicated by a blue arrow. Using this procedure for 16 different normalized spectra leads to an average CDW gap $2\Delta = (24 \pm 6)$ meV. This value is smaller than our resolution near T_C due to thermal broadening [41], hindering us to extract the DOS above T_C instead of using the polynomial fit.

Based on previous ARPES measurements [11,21,22], CDWs in VSe_2 arise from FS nesting in the electron pockets around the M points of the Brillouin zone along directions

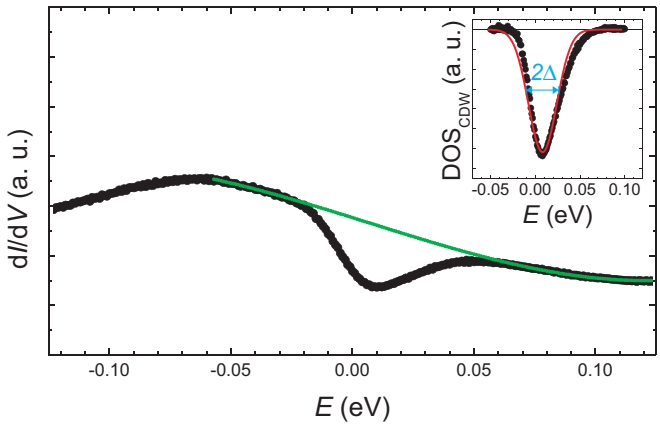

FIG. 5. CDW gap in STS spectra: High-resolution STS spectrum of VSe_2 ($U_{stab} = 0.2$ V, $I_{stab} = 3.2$ nA). We find again the features mentioned above, with a pronounced gap around the Fermi level. The green dots represent a third-order polynomial fit to the data in the vicinity of the Fermi energy, but neglecting the gap. The inset shows the difference between the STS spectrum and the polynomial fit, DOS_{CDW}, which is then fitted with a Gaussian (red) to extract the CDW gap 2Δ from its FWHM.

between two neighboring M points and with a non-negligible out-of-plane component. In this scenario, the DOS at the Fermi energy is reduced due to nesting but still finite, since not all states contribute to CDW formation. The fact that no decrease of the DOS to zero over a finite energy range, i.e., no true gap, is found in our STS spectra can be attributed to this scenario, where the suppression of the DOS at the chemical potential is limited to states corresponding to the nesting vector.

IV. THE ROLE OF DEFECTS

The influence of defects is of great importance in VSe_2, as it is possible to produce stable nonstoichiometric compounds [42]. Nonstoichiometric compositions of $V_{1+x}Se_2$ with $x =$ 0.01 0.28 have been reported [43], in which the excess V is located in the van der Waals gap between two Se layers as interstitials [43].

Impurities can be modeled as potential scatterers that tend to pin the CDW phase [44]. One can define two different regimes: the *strong pinning regime* with strong impurity potential or a low impurity concentration, and *the weak pinning regime* that applies when the impurity potential is weak or the impurity concentration is high [44]. In both cases, the CDW periodicity is perturbed near defects, where it can minimize the impurity energy by matching its phase to the impurity location, at the cost of elastic energy due to the resulting distortion. CDW pinning is reported to play an important role for the CDWs properties in $NbSe_2$ [45] and doped $NbSe_3$ [46], as well as in the formation of the CDW phase at the ultrathin Sn/Ge(111)-α interface [47].

The effect of defects in VSe_2 is investigated by analyzing different batches of VSe_2 with varying defect concentration. The defects are point defects such as Se vacancies or V interstitials, but they could also stem from the transport agent used for sample preparation. Figure 6(a) shows an STM image with a moderate concentration of defects. The upper left part of the image, which is essentially defect-free, shows a pronounced, symmetric (4×4) periodicity due to the CDW formation. The CDW periodicity is also well visible in the FT

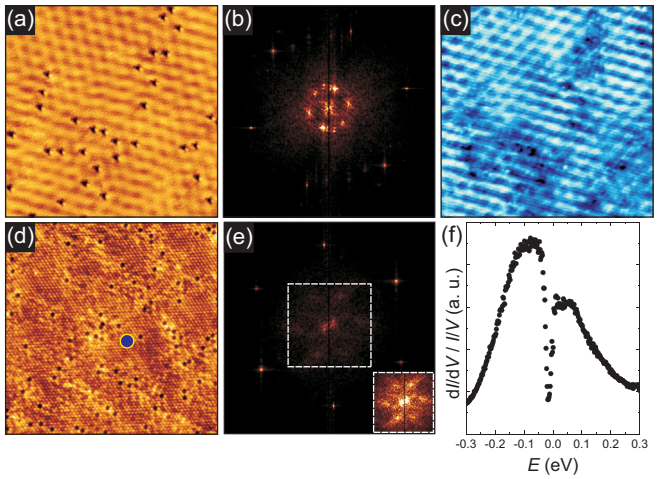

FIG. 6. Defects in VSe_2: (a) STM image containing both point defects and the CDW ($U = -0.3$ V, $I = 0.21$ nA, image size 20×20 nm^2). The number of defects per (1×1) unit cell amounts to 0.8%. (b) FT of (a). The spot corresponding to the atomic lattice and the CDW are well visible. (c) Corresponding STS map recorded at $U = -0.05$ V. (d) STM image from a VSe_2 crystal with a large defect density amounting to 2.0% ($U = 0.355$ V, $I = 0.1$ nA, image size 20×20 nm^2). (e) FT of (d), showing six sharp spots corresponding to the atomic lattice. Six diffuse features rotated by 30° become visible when enhancing the contrast; see the inset. (f) Normalized STS spectrum measured at the position marked by a blue dot in (d), showing a pronounced CDW gap, although the CDW is barely visible at the location of the spectrum acquisition ($U_{\text{stab}} = 0.5$ V, $I_{\text{stab}} = 0.2$ nA).

of Fig. 6(a) shown in Fig. 6(b). It is strongly perturbed near defects, resulting in a distorted wave pattern. The perturbation is also visible in STS maps taken at the same location; see Fig. 6(c). The energy is chosen to be near the CDW gap since this is the energy where one expects the standing-wave pattern to be most pronounced due to the selected (nesting) wave vector. The CDW periodicity is most visible in the defect-free region, while it is disturbed near the defects such as in the right and lower part of the image. These observations clearly show that defects strongly influence the phase and order of the CDW in VSe_2. According to Ref. [44], the attenuation in the LDOS points to weak pinning instead of strong pinning, which is also plausible because of the high concentration of defects in the image.

It is possible to perturb the ordered appearance of the CDW on the surface of VSe_2 even further by increasing the defect concentration as shown in Fig. 6(d), where a sample from a second batch with a larger defect concentration was imaged. The defects induce an incoherent pattern on the surface due to the pinning of the CDW phase at the defects [44]. While a CDW periodicity is barely visible in real space, we still find a sixfold superperiodicity in the corresponding FT shown in Fig. 6(e). This superperiodicity is rotated by 30° compared to the undisturbed CDW of VSe_2, it has a larger wave vector, and it is blurred. One possible speculation is that due to interstitial defects the layers become decoupled, whereby the most favorable nesting condition and hence the orientation of the CDW with respect to the lattice is modified.

Interestingly, the CDW gap in the DOS is, within the limits of our experimental error, unaffected, as shown in Fig. 6(f). The spectrum is taken at the blue dot of Fig. 6(d) and shows a pronounced gap in $dI/dV/I/V$ that is in agreement (within error margin) with CDW gaps taken on defect-free areas of samples with an overall low defect concentration. This leads to the conclusion that although defects act as local potential scatterers that affect the phase coherence of the CDW, they barely influence the stability of the CDW and its corresponding phase transition. These findings agree with reported ion bombardment experiments on VSe_2 [42], which found that the phase transition only reduces from 110 K to around 80 K when introducing a fraction of 10^{-2} displaced metal atoms [48].

V. DISCUSSION

The electronic properties of VSe_2 that are accessible with STS spectra are twofold. First, one is able to resolve the rich structure of the VSe_2 DOS. The strong deviation between STS and the tight-binding model in the unoccupied DOS reveals the need to probe both occupied and unoccupied states to get a complete and reliable picture of the band structure and resulting DOS of VSe_2. The flat band at the Γ point near the Fermi level is the most pronounced feature in STS spectra due to its vanishing $k_{||}$.

In addition, we find a pronounced suppression in the DOS around the Fermi level that is attributed to the CDW formation at low temperatures. This partial gap is located very near to the peak of the flat VSe_2 band. The latter can easily be mistaken as one of the edges of the CDW gap, an issue that is likely the main reason for the strong scatter of the CDW gap 2Δ reported in STS experiments [23,24]. Only with the knowledge of the DOS of VSe_2 and for spectra taken at sufficiently high energy resolution (low temperatures) may one be able to extract the CDW gap by subtracting the contribution of the undistorted VSe_2 DOS. Another important aspect of the CDW gap is that it lacks a sharp edge in STS spectra, presumably due to the small fraction of the FS involved in the CDW gap opening. This makes a quantitative analysis difficult. Our way of analyzing the size of the CDW gap is therefore just an estimate, but obtainable in a well-defined and reproducible procedure.

Assuming weak electron-phonon coupling, one may estimate a CDW temperature using the measured CDW gap $2\Delta = (24 \pm 6)$ meV. Using a BCS-like relation [3], the transition temperature T_C of VSe_2 is given by

$$T_C = \frac{2\Delta}{3.52 k_B} = (80 \pm 20)\,\text{K}. \quad (1)$$

This value is in good agreement with the experimental transition temperatures of VSe_2, which are at 110 K (incommensurate) and 80 K (commensurate). Weak electron-phonon coupling is also in line with ARPES measurements, which show only small changes, if any, in the band structure when crossing T_C, and no replica bands that would be expected when the electron-phonon coupling would be strong [11,21,22].

Assuming that the electron-phonon coupling is weak, Pásztor *et al.* [17] proposed that a measure based on the CDW modulation amplitude normalized to the atomic modulation,

which is proportional to the CDW gap in the mean-field approximation [49], can be used as an order parameter to obtain the transition temperature and CDW gap of VSe_2. Using this methodology, Pásztor *et al.* derived the thickness-dependent transition temperature of VSe_2 in a convincing way. Our results point to additional effects that act on the modulation amplitudes: (i) The tip apex can influence the ratio between atomic and CDW amplitude, and (ii) the CDW amplitude is strongly reduced near defects. The first effect potentially leads to stronger variation than that due to local changes of the CDW transition temperature alone. Therefore, using the STM measured CDW amplitude as an order parameter requires precautions to ensure identical tip states in different measurements. The second effect produces a systematic error, leading to an underestimation for the CDW transition temperature. Hence, when defects are present, the measured CDW gap is likely to give a more accurate measure for the transition temperature. This is because the CDW gap is still present and apparently unaffected in the presence of defects, while the CDW modulation and order are strongly modified.

VI. CONCLUSIONS

In conclusion, as a measure for the partial CDW gap, we determine the FWHM of the associated dip in the DOS of our STS spectra at the chemical potential to be $2\Delta = (24 \pm 6)$ meV. This estimate of the gap size is in line with the actual CDW transition temperature assuming weak electron-phonon coupling in VSe_2. The gap analysis was based on the experimental band structure known from ARPES to which we fitted a tight-binding model that allowed us to calculate the related DOS. By comparison, we identified peaks in the STS spectra related to p- and d-derived VSe_2 states. This procedure enabled us to differentiate between band-structure-related features and the partial gap opening. The applied methodology may help to adequately interpret tunneling spectra of other CDW materials with partial CDW gaps. Finally, the CDWs of VSe_2 are shown to be preserved even at high defect densities, though the CDW appearance, order, and local phase are strongly perturbed, presumably due to weak pinning. A systematic study on how the defects affect the electronic properties of VSe_2 and the CDW would be desirable future work.

ACKNOWLEDGMENTS

The authors acknowledge funding by the Deutsche Forschungsgemeinschaft (DFG, German Research Foundation) - Project Number 277146847 - CRC 1238 (subprojects A01 and B06), and A.G., N.E., as well as K.N. additionally through project GR 3708/2-1. W.J. acknowledges support from the Bonn-Cologne Graduate School for Physics and Astronomy. A.G., N.E., and K.N. also acknowledge support from the ERC Grant No. 648589 SUPER-2D.

[1] R. E. Peierls, *Quantum Theory of Solids* (Clarendon, Oxford, 1955).
[2] X. Xi, L. Zhao, Z. Wang, H. Berger, L. Forró, J. Shan, and K. F. Mak, Nat. Nanotechnol. **10**, 765 (2015).
[3] K. Rossnagel, J. Phys.: Condens. Matter **23**, 213001 (2011).
[4] T. Ritschel, J. Trinckauf, K. Koepernik, B. Büchner, M. V. Zimmermann, H. Berger, Y. I. Joe, P. Abbamonte, and J. Geck, Nat. Phys. **11**, 328 (2015).
[5] Y. Liu, D. F. Shao, L. J. Li, W. J. Lu, X. D. Zhu, P. Tong, R. C. Xiao, L. S. Ling, C. Y. Xi, L. Pi, H. F. Tian, H. X. Yang, J. Q. Li, W. H. Song, X. B. Zhu, and Y. P. Sun, Phys. Rev. B **94**, 045131 (2016).
[6] M. Porer, U. Leierseder, J.-M. Ménard, H. Dachraoui, L. Mouchliadis, I. E. Perakis, U. Heinzmann, J. Demsar, K. Rossnagel, and R. Huber, Nat. Mater. **13**, 857 (2014).
[7] X. Xi, H. Berger, L. Forró, J. Shan, and K. F. Mak, Phys. Rev. Lett. **117**, 106801 (2016).
[8] S. He, H. Lin, L. Qin, Z. Mao, H. He, Y. Li, and Q. Li, J. Mater. Chem. A **5**, 2163 (2016).
[9] J. Gao, X. Di, W. Li, L. Feng, J. Zhang, L. Wu, B. Li, W. Wang, G. Zeng, and J. Yang, Thin Solid Films **550**, 638 (2014).
[10] A. Ghobadi, T. G. U. Ghobadi, A. K. Okyay, and E. Ozbay, Photon. Res. **6**, 244 (2018).
[11] V. N. Strocov, M. Shi, M. Kobayashi, C. Monney, X. Wang, J. Krempasky, T. Schmitt, L. Patthey, H. Berger, and P. Blaha, Phys. Rev. Lett. **109**, 086401 (2012).
[12] J. Mahy, J. Van Landuyt, and S. Amelinckx, Phys. Status Solidi **74**, K89 (1982).
[13] K. Tsutsumi, Phys. Rev. B **26**, 5756 (1982).
[14] D. J. Eaglesham, R. L. Withers, and D. M. Bird, J. Phys. C **19**, 359 (1986).
[15] J. Yang, W. Wang, Y. Liu, H. Du, W. Ning, G. Zheng, C. Jin, Y. Han, N. Wang, Z. Yang, M. Tian, and Y. Zhang, Appl. Phys. Lett. **105**, 063109 (2014).
[16] K. Xu, P. Chen, X. Li, C. Wu, Y. Guo, J. Zhao, X. Wu, and Y. Xie, Angew. Chem., Int. Ed. Engl. **52**, 10477 (2013).
[17] Á. Pásztor, A. Scarfato, C. Barreteau, E. Giannini, and C. Renner, 2D Mater. **4**, 041005 (2017).
[18] M. Bonilla, S. Kolekar, Y. Ma, H. C. Diaz, V. Kalappattil, R. Das, T. Eggers, H. R. Gutierrez, M.-H. Phan, and M. Batzill, Nat. Nanotechnol. **13**, 289 (2018).
[19] J. Feng, D. Biswas, A. Rajan, M. D. Watson, F. Mazzola, O. J. Clark, K. Underwood, I. Marković, M. McLaren, A. Hunter, D. M. Burn, L. B. Duffy, S. Barua, G. Balakrishnan, F. Bertran, P. Le Fèvre, T. K. Kim, G. van der Laan, T. Hesjedal, P. Wahl, and P. D. C. King, Nano Lett. **18**, 4493 (2018).
[20] G. Duvjir, B. K. Choi, I. Jang, S. Ulstrup, S. Kang, T. T. Ly, S. Kim, Y. H. Choi, C. Jozwiak, A. Bostwick, E. Totenberg, J.-G. Park, R. Sankar, K.-S. Kim, J. Kim, and Y. J. Chang, Nano Lett. **18**, 5432 (2018).
[21] K. Terashima, T. Sato, H. Komatsu, T. Takahashi, N. Maeda, and K. Hayashi, Phys. Rev. B **68**, 155108 (2003).
[22] T. Sato, K. Terashima, S. Souma, H. Matsui, T. Takahashi, H. Yang, S. Wang, H. Ding, N. Maeda, and K. Hayashi, J. Phys. Soc. Jpn. **73**, 3331 (2004).

[23] C. Wang, C. G. Slough, and R. V. Coleman, J. Vac. Sci. Technol. B **9**, 1048 (1991).
[24] I. Ekvall, H. E. Brauer, E. Wahlström, and H. Olin, Phys. Rev. B **59**, 7751 (1999).
[25] R. Coleman, B. Giambattista, P. Hansma, A. Johnson, W. McNairy, and C. Slough, Adv. Phys. **37**, 559 (1988).
[26] B. Giambattista, C. G. Slough, W. W. McNairy, and R. V. Coleman, Phys. Rev. B **41**, 10082 (1990).
[27] J. J. Kim, C. Park, and H. Olin, J. Kor. Phys. Soc. **31**, 713 (1997).
[28] T. Ohtani, H. Nakamura, M. Nakahira, and M. Ishii, J. Less-Common Met. **77**, 185 (1981).
[29] K. S. Nikonov, M. N. Brekhovskikh, A. V. Egorysheva, T. K. Menshchikova, and V. A. Fedorov, Inorg. Mater. **53**, 1126 (2017).
[30] K. Besocke, Surf. Sci. **181**, 145 (1987).
[31] I. Horcas, R. Fernández, J. M. Gómez-Rodríguez, J. Colchero, J. Gómez-Herrero, and A. M. Baro, Rev. Sci. Instrum. **78**, 013705 (2007).
[32] L. Petaccia, P. Vilmercati, S. Gorovikov, M. Barnaba, A. Bianco, D. Cocco, C. Masciovecchio, and A. Goldoni, Nucl. Instrum. Methods Phys. Res., Sect. A **606**, 780 (2009).
[33] See Supplemental Material at http://link.aps.org/supplemental/10.1103/PhysRevB.99.115417 for additional ARPES results.
[34] N. Ehlen *et al.* (unpublished).
[35] E. Cappelluti, R. Roldán, J. A. Silva-Guillén, P. Ordejón, and F. Guinea, Phys. Rev. B **88**, 075409 (2013).
[36] E. Ridolfi, D. Le, T. S. Rahman, E. R. Mucciolo, and C. H. Lewenkopf, J. Phys.: Condens. Matter **27**, 365501 (2015).
[37] J. C. Slater and G. F. Koster, Phys. Rev. **94**, 1498 (1954).
[38] R. M. Feenstra, J. A. Stroscio, and A. P. Fein, Surf. Sci. **181**, 295 (1987).
[39] B. Voigtländer, *Scanning Probe Microscopy* (Springer, Berlin, 2015).
[40] H. E. Brauer, H. I. Starnberg, L. J. Holleboom, V. N. Strocov, and H. P. Hughes, Phys. Rev. B **58**, 10031 (1998).
[41] M. Morgenstern, Surf. Rev. Lett. **10**, 933 (2003).
[42] H. Mutka and P. Molinie, J. Phys. C **15**, 6305 (1982).
[43] K. Hayashi and M. Nakahira, J. Solid State Chem. **24**, 153 (1978).
[44] H. Fukuyama and P. A. Lee, Phys. Rev. B **17**, 535 (1978).
[45] C. J. Arguello, S. P. Chockalingam, E. P. Rosenthal, L. Zhao, C. Gutiérrez, J. H. Kang, W. C. Chung, R. M. Fernandes, S. Jia, A. J. Millis, R. J. Cava, and A. N. Pasupathy, Phys. Rev. B **89**, 235115 (2014).
[46] J. McCarten, D. A. DiCarlo, M. P. Maher, T. L. Adelman, and R. E. Thorne, Phys. Rev. B **46**, 4456 (1992).
[47] H. H. Weitering, J. M. Carpinelli, A. V. Melechko, J. Zhang, M. Bartkowiak, and E. W. Plummer, Science **285**, 2107 (1999).
[48] H. Mutka, N. Housseau, J. Pelissier, R. Ayroles, and C. Roucau, Solid State Commun. **50**, 161 (1984).
[49] G. Grüner, *Density Waves in Solids* (Westview, Boulder, CO, 2000).